Electronic structure of *R*Sb (*R* = Y, Ce, Gd, Dy, Ho, Tm, Lu) studied by angle-resolved photoemission spectroscopy

Yun Wu,[1,2] Yongbin Lee,[1] Tai Kong,[1,2,*] Daixiang Mou,[1,2] Rui Jiang,[1,2] Lunan Huang,[1,2] S. L. Bud'ko,[1,2] P. C. Canfield,[1,2,†] and Adam Kaminski[1,2,‡]

[1]*Division of Materials Science and Engineering, Ames Laboratory, Ames, Iowa 50011, USA*

[2]*Department of Physics and Astronomy, Iowa State University, Ames, Iowa 50011, USA*

(Received 20 April 2017; revised manuscript received 21 June 2017; published 19 July 2017)

We use high-resolution angle-resolved photoemission spectroscopy (ARPES) and electronic structure calculations to study the electronic properties of rare-earth monoantimonides *R*Sb (*R* = Y, Ce, Gd, Dy, Ho, Tm, Lu). The experimentally measured Fermi surface (FS) of *R*Sb consists of at least two concentric hole pockets at the Γ point and two intersecting electron pockets at the *X* point. These data agree relatively well with the electronic structure calculations. Detailed photon energy dependence measurements using both synchrotron and laser ARPES systems indicate that there is at least one Fermi surface sheet with strong three-dimensionality centered at the Γ point. Due to the "lanthanide contraction", the unit cell of different rare-earth monoantimonides shrinks when changing the rare-earth ion from CeSb to LuSb. This results in the differences in the chemical potentials in these compounds, which are demonstrated by both ARPES measurements and electronic structure calculations. Interestingly, in CeSb, the intersecting electron pockets at the *X* point seem to be touching the valence bands, forming a fourfold-degenerate Dirac-like feature. On the other hand, the remaining rare-earth monoantimonides show significant gaps between the upper and lower bands at the *X* point. Furthermore, similar to the previously reported results of LaBi, a Dirac-like structure was observed at the Γ point in YSb, CeSb, and GdSb, compounds showing relatively high magnetoresistance. This Dirac-like structure may contribute to the unusually large magnetoresistance in these compounds.

DOI: 10.1103/PhysRevB.96.035134

I. INTRODUCTION

Rare-earth monoantimonides *R*Sb (*R* denotes rare earth) have attracted a great deal of attention due to their remarkable magnetic and electronic properties [1–5]. Although these compounds crystallize in the simple NaCl-type cubic structure [1], most of them exhibit strongly anisotropic magnetic properties below their Néel temperatures [2,3,6]. TbSb, HoSb, and ErSb become antiferromagnetic at low temperature, showing the MnO-type arrangement of magnetic moments, i.e., with ferromagnetic sheets perpendicular to the cube diagonal, and magnetic moments in adjacent sheets arranged in an antiparallel way [1]. Most of the *R*Sb (except for GdSb) studied by Busch *et al.* [2] show metamagnetic properties, i.e., the spin structure changes abruptly from antiferromagnetism to a spin arrangement with a net magnetic moment under sufficiently high magnetic fields. Further studies [6] of these compounds show that strong anisotropy is found in the monoantimonides of Ce, Nd, Dy, and Ho (in agreement with the Ising model), whereas TbSb and ErSb only exhibit weak anisotropy. DySb has been shown to have a single first-order magnetic phase transition through specific-heat, susceptibility, and neutron scattering measurements [7]. Among these compounds, CeSb has the most complicated magnetic phase diagram with at least 14 distinct metamagnetic states at low temperatures and magnetic fields [4,8]. In CeSb, the largest observable Kerr rotation (90°) in a single reflection has also been reported [9]. Recently, extremely large magnetoresistance [10–13] has attracted tremendous attention. Not only do the materials with this type of property have potential applications such as magnetic field sensors, but they are also platforms for studying exotic physical properties, such as Dirac node arc states [14], type-II Weyl fermion states [15–19], three-dimensional Dirac states [20–23], etc. Interestingly, CeSb also shows a relatively high magnetoresistance of 9000% at 5 K and 5.5 T [8]. In addition to CeSb, GdSb shows even higher magnetoresistance, reaching 1.25×10^4% at 4.2 K and 10 T [24]. All the research indicates that different rare-earth elements would have different impacts on the electronic and magnetic properties of these compounds. If we are measuring the electronic properties of these compounds at $T > T_N$, the different ionic sizes (due to lanthanide contraction) may have a significant effect on the electronic structure of these materials. Thus, in order to understand the role that lanthanide contraction plays in these compounds, detailed electronic structure measurements of *R*Sb are necessary.

A number of electronic properties of *R*Sb were previously studied using band-structure calculations [25–32], quantum oscillations [33,34], and angle-resolved photoemission spectroscopy (ARPES) measurements [35–40]. However, systematic ARPES studies of the rare-earth monoantimonides, especially photon-energy-dependent measurements, are still needed to better understand these materials. Here, we present a study of the Fermi surface and band dispersion of *R*Sb (*R* = Y, Ce, Gd, Dy, Ho, Tm, Lu), with specific emphasis on their three-dimensional (3D) character, using high-resolution synchrotron and tunable VUV laser ARPES measurements. The FS of *R*Sb consists of at least two hole pockets at the Γ

*Present address: Department of Chemistry, Princeton University, Princeton, NJ 08544.

†canfield@ameslab.gov

‡kaminski@ameslab.gov

TABLE I. Physical properties of *R*Sb (*R* denotes rare earth).

*R*Sb	Lattice a (Å)[a]	Ionic radii (Å)[b]	T_N (K)[c]
YSb	6.190	0.9[d]	
CeSb	6.408	1.01	16.7[e]
GdSb	6.210	0.938	28
DySb	6.150	0.912	9.5[f]
HoSb	6.130	0.901	5.5[g]
TmSb	6.090	0.88	
LuSb	6.060	0.86	

[a,b,c,d,e] Data from Refs. [2,8,42–44].
[f]Reference [45] reported a value of 12 K.
[g]Reference [1] reported a value of 9 K.

point and two, intersecting, electron pockets at the X point. We also determined the band structure at the Γ point along the out-of-plane (k_z) direction, which shows strong three-dimensionality. Interestingly, a fourfold-degenerate Dirac-like feature was observed at the X point in CeSb, consistent with the previously reported results [41]. However, other compounds, such as GdSb and YSb, show significant gaps between the conduction and valence bands at the X point. Furthermore, a Dirac-like feature is observed at the Γ point within a specific photon energy range in YSb, CeSb, and GdSb, which may contribute to the unusually high magnetoresistance observed in these compounds.

II. EXPERIMENTAL DETAILS

Single crystals of *R*Sb were grown either from a tin-rich ternary melt [46] for the light rare earths, or from an antimony-rich binary solution for the heavy rare earths [47]. In all cases, high-purity elements were placed into an alumina crucible, which itself was sealed into an amorphous silica ampoule, heated to above 1000 °C, and then slowly cooled to a decanting temperature at which point the ampoule was placed into a centrifuge and excess solution was removed from the crystals [46,47]. We present a summary of the key physical properties of *R*Sb crystals in Table I. These data nicely demonstrate the lanthanide contraction effect.

The full-potential linear augmented plane wave (FPLAPW) method [48] with the generalized gradient approximation (GGA) [49] was used to calculate the theoretical FS. The spin-orbit interaction was included. To obtain self-consistent charge density, we employed $R_{\mathrm{MT}} \times k_{\mathrm{max}} = 8.0$ with muffin tin (MT) radii of 2.8 and 2.7 a.u. for Lu, and Sb, respectively. 315 k-points were selected in the irreducible Brillouin zone and calculations were iterated to reach the total energy convergence criterion, which was 0.01 mRy/cell. For Fermi surface calculations, we divided the $-2\pi/a < k_x, k_y < 2\pi/a$ range of the k_x, k_y planes with different k_z values by a 200×200 mesh. Figure 2(a) (below) is the result of $k_z = 0$. Since it is convenient to compare with experiment results, we have used a reduced unit cell ($a = b = 4.285$ Å, $c = 6.060$ Å) for calculations.

Fermi surfaces of YSb, CeSb, GdSb, and LuSb were measured at the Advanced Light Source (ALS) synchrotron based ARPES system, utilizing a Scienta SES2002 electron analyzer. Momentum and energy resolutions were set at 0.014 Å^{-1} along the direction of the analyzer slits and 17 meV, respectively. The samples were cleaved at temperatures around 20 K and kept at their cleaving temperatures throughout the measurements. k_z measurements of YSb and CeSb were carried out at the Synchrotron Radiation Center (SRC) at Wisconsin with an ARPES system consisting of an R4000 electron analyzer. Detailed k_z mappings of YSb, DySb, HoSb, TmSb, and LuSb were performed using a tunable VUV laser ARPES system consisting of a Scienta R8000 electron analyzer, a picosecond Ti:sapphire oscillator, and a fourth-harmonic generator [50]. Samples were cleaved *in situ* at 40 K under ultrahigh vacuum (UHV) and kept at their cleaving temperatures throughout the measurements. Data were collected with tunable photon energies in the 5.3–6.7 eV range. Momentum and energy resolutions were set at ∼0.005 Å^{-1} and 1 meV, respectively. The size of the photon beam on the sample was ∼30 μm.

III. EXPERIMENTAL RESULTS

In Figs. 1(a)–1(d), we show the Fermi surface intensity plots of *R*Sb (R = Ce, Gd, Y, Lu) integrated within 10 meV about the chemical potential measured at the corresponding temperatures and photon energies as marked at the top left and right corners of each plot. In panel (a), we can see that there are at least two pockets at the Γ point in CeSb; however, we cannot resolve these two pockets with confidence in other rare-earth compounds, as shown in panels (b), (c), and (d). At the X point, two elongated electron pockets can be clearly seen in Figs. 1(a), 1(b) and 1(c). In panel (d), the FS of LuSb clearly shows fourfold symmetry, consistent with the simple cubic structure of the compound, although the relative intensity of each electron pocket varies due to the matrix elements. The structures of the Fermi surfaces for these different compounds are quite similar, with at least two hole pockets at the center and two electron pockets at each corner of the Brillouin zone. These results confirm that the increased number of 4f electrons in the rare-earth elements does not have a significant effect on the electronic structure of the *R*Sb system near E_F. Thus the 4f electrons are likely strongly localized, and shielded by the completely filled $5s^2$, $5p^6$, and $6s^2$ shells. However, the differences in the other aspects of the band structure are also obvious. The size of the pockets in these compounds seems to be different, which may be due to the differences in the chemical potential. However, no solid conclusion can be drawn from this set of data since they are FS sheets measured at different k_z as marked by the red dashed lines in Fig. 4. More detailed results and analysis will be provided in the laser ARPES measurements as discussed below using much higher energy and momentum resolutions. In panels (d1)–(d4), we show the constant energy contour plots of LuSb at the binding energies of 0.3, 0.5, 0.9, and 1.5 eV. As we move down from the chemical potential [panel (d)] to the binding energy of 0.3 eV [panel (d1)], we can clearly see that the constant energy intensity contours at the Γ point expand, and the ones at the X point shrink, demonstrating the hole and electron character of the Fermi pockets at the Γ and X point, respectively. In panel (d2), an additional band with a circular constant energy contour is detected at the Γ point, and the electron pockets at the X point completely vanish. As we move further down to 0.9 eV, the constant energy contour at the Γ point continues to

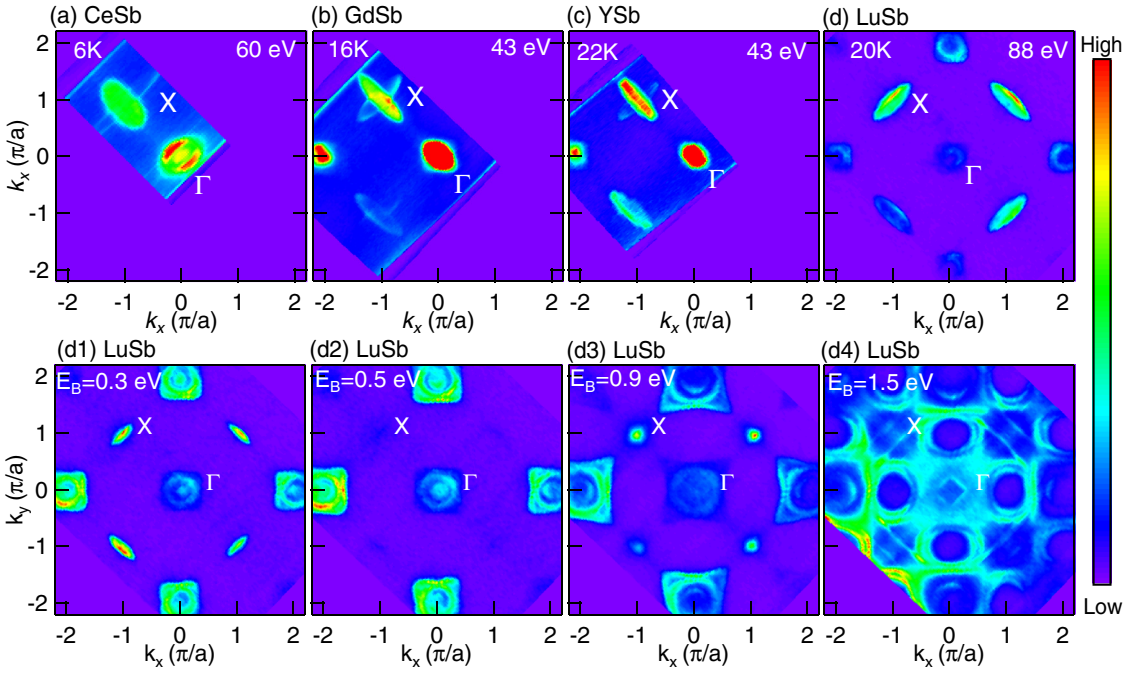

FIG. 1. Constant energy contour plots of RSb (R = Ce, Gd, Y, and Lu). (a)–(d) Fermi surface plots of ARPES intensity integrated within 10 meV about the chemical potential, corresponding to CeSb, GdSb, YSb, and LuSb, respectively. The specific temperature and incident photon energy used during the measurements are marked at the top left and right corners, respectively. (d1)–(d4) Constant energy contour plots of LuSb measured using the photon energy of 88 eV at the binding energies of 0.3, 0.5, 0.9, and 1.5 eV, respectively.

expand, and a new feature is detected at the X point. Panel (d4) shows that the constant energy contour at high binding energy is rather complex yet still highly symmetric with fourfold symmetry.

Figures 2(a)–2(c) and 2(d)–2(f) show the calculated Fermi surface and band structure of YSb, GdSb, and LuSb. A similar Fermi surface and band structure clearly can be seen across these crystals. We note that both the ARPES data shown here and calculation results [28] for CeSb are similar to other members of this family. However, the chemical potential is different, as shown in Fig. 2(g). Minor differences in the chemical potentials can be seen between YSb and GdSb, which have similar lattice constants. On the other hand, GdSb and LuSb show significant differences in chemical potential.

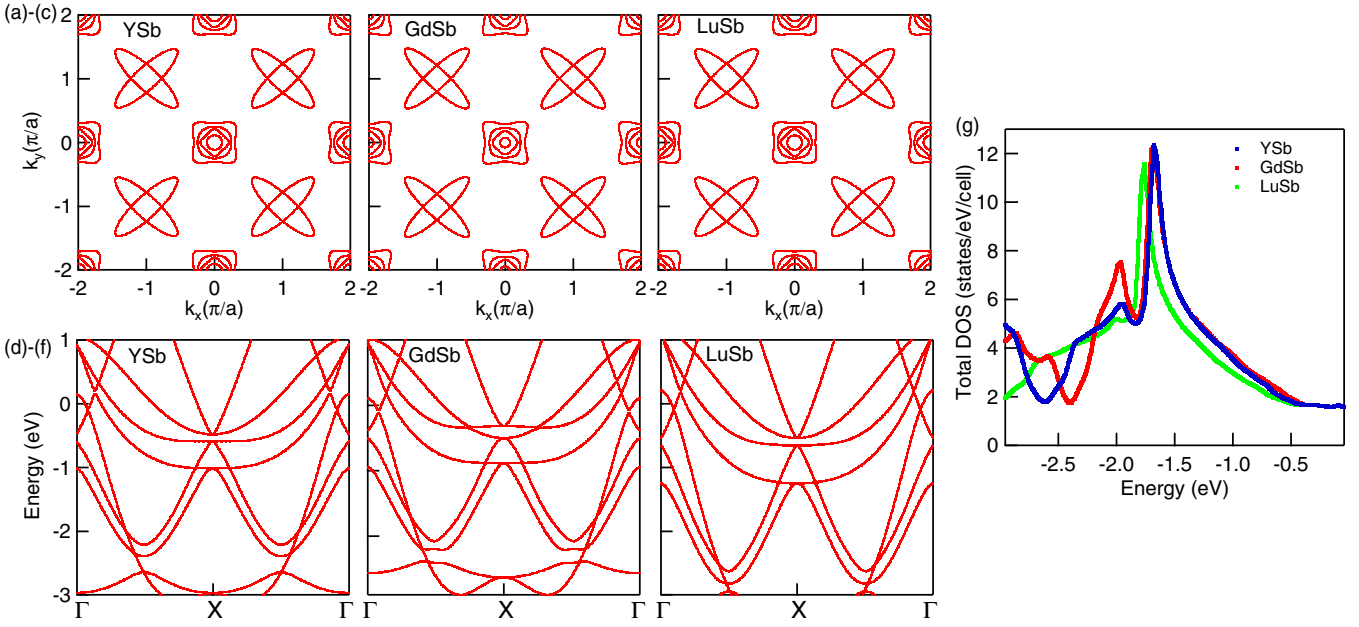

FIG. 2. Calculated Fermi surface and band dispersion of YSb, GdSb, and LuSb. (a)–(c) Calculated Fermi surface of YSb, GdSb, and LuSb. (d)–(f) Calculated band structure along Γ-X of YSb, GdSb, and LuSb. (g) Calculated density of states (DOS) of YSb, GdSb, and LuSb

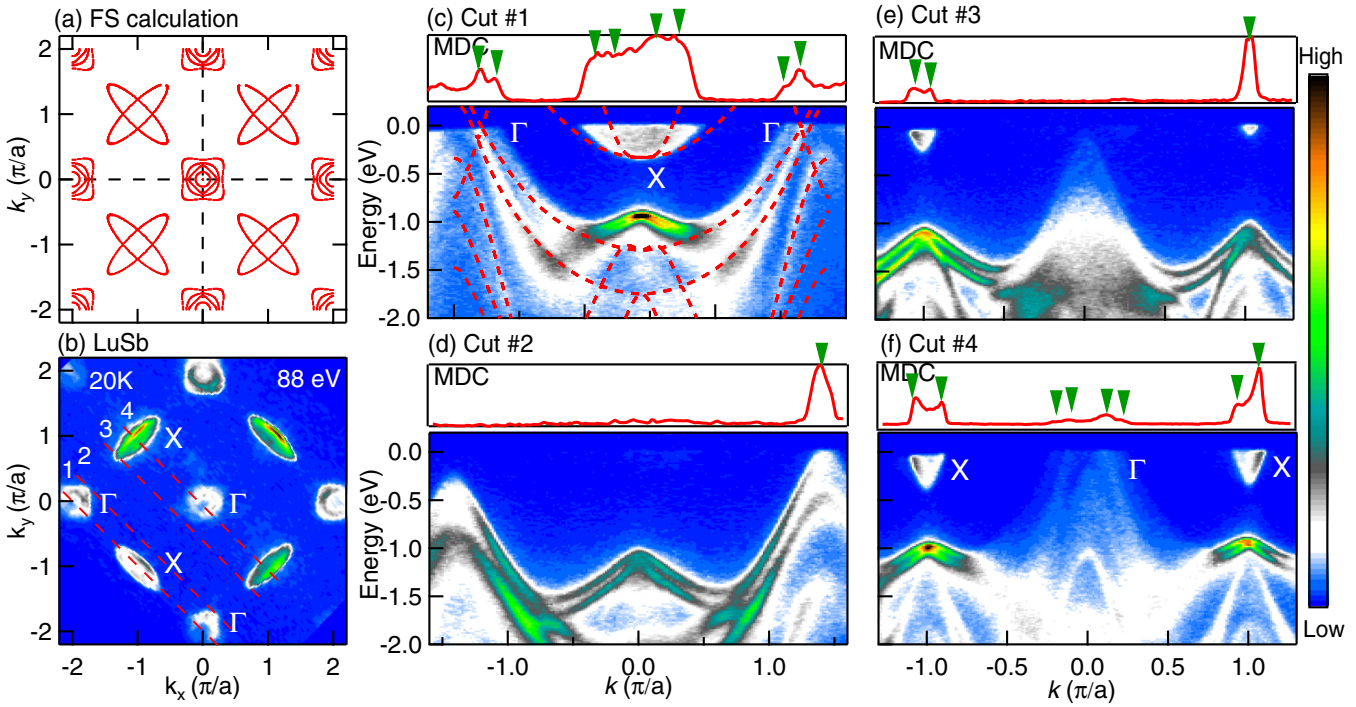

FIG. 3. Fermi surface and band dispersion of LuSb measured at $T = 20$ K and photon energy of 88 eV. (a) Calculated Fermi surface using the FPLAPW method. (b) Fermi surface plot of ARPES intensity integrated within 10 meV about the chemical potential of LuSb measured at $T = 20$ K and photon energy of 88 eV. (c)–(f) Band dispersion along cuts 1–4 in panel (b). The top panels show the momentum dispersion curves (MDCs) at the Fermi level. The green arrows point to the obvious Fermi crossings. The red dashed lines in panel (c) are the results from band-structure calculations.

Later, we also will show ultrahigh-resolution laser ARPES measurements to demonstrated this in Fig. 5.

Figure 3(a) shows the calculated FS of *R*Sb at the chemical potential ($k_z = 0$), with two circular pockets and two squarish pockets at the Γ point. At the *X* point, two elongated pockets intersect, similar to the nodal ring structures that were proposed to exist in lanthanum monopnictides [51]. Panel (b) shows the FS of LuSb measured using a photon energy of 88 eV,

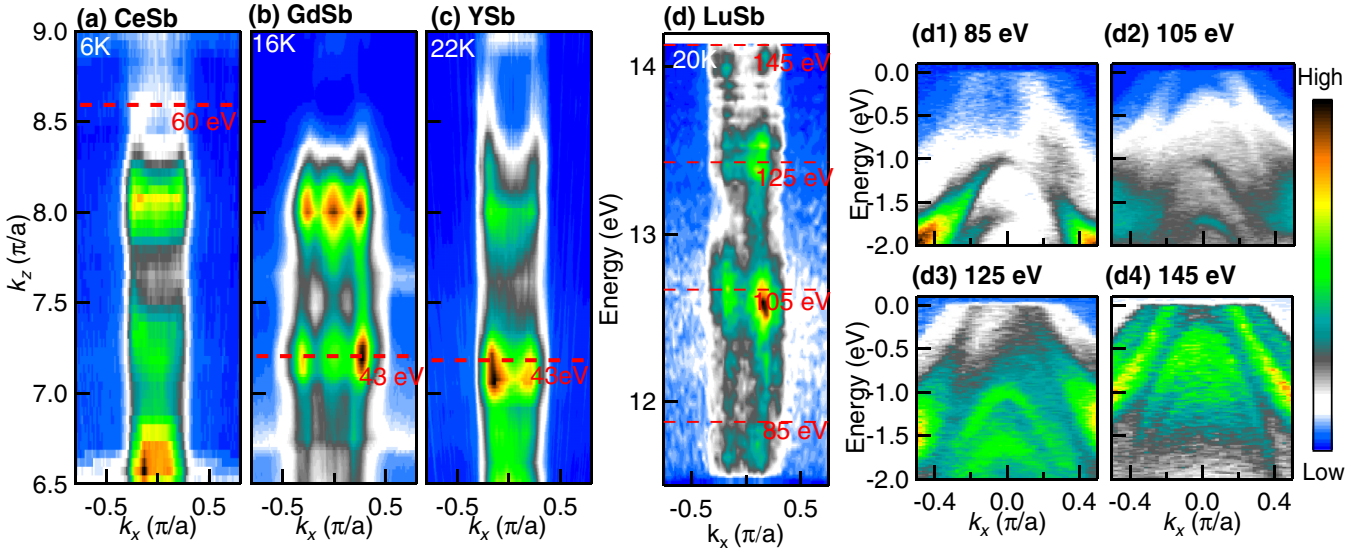

FIG. 4. Out-of-plane momentum (k_z) dispersion of YSb, CeSb, GdSb, and LuSb at the Γ point measured using photon energies in the 20–150 eV range. The corresponding temperatures during the measurements are marked at the top left corner in each plot. (a) k_z dispersion of CeSb measured at SRC using photon energies in the 30–80 eV range with 2 eV steps. (b) k_z dispersion of GdSb measured at ALS using photon energies in the 20–80 eV range with 1 eV steps. (c) k_z dispersion of YSb measured at SRC using photon energies in the 30–76 eV range with 2 eV steps. (d) k_z dispersion of LuSb measured at ALS using photon energies in the 77–145 eV range with 1 eV steps. (d1)–(d4) Band dispersion of LuSb at the Γ point measured using the corresponding incident photon energies.

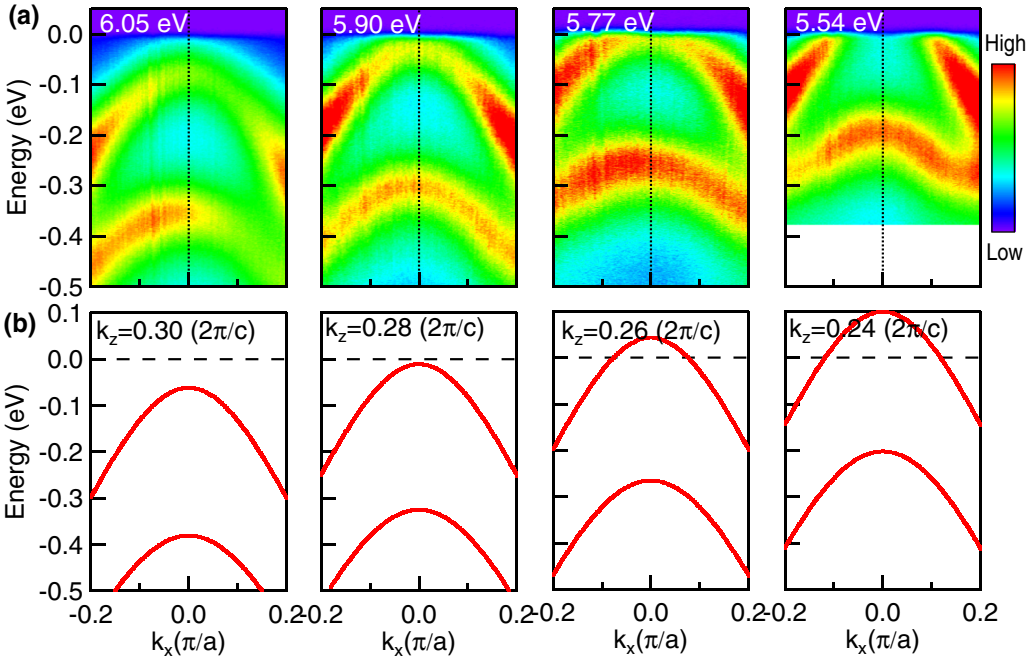

FIG. 5. Band dispersion of YSb at the Γ point measured at $T = 40$ K and using different photon energies. (a) Band dispersion of YSb measured using various photon energies marked at the top of each plot. (b) Calculated band dispersion of YSb at various k_z values marked at the top of each plot.

which matches relatively well the calculated FS shown in Fig. 3(a). The other elongated electron pocket at the X point is not clearly visible in LuSb, most likely due to the effect of matrix elements. On the other hand, those intersecting elongated electron pockets in CeSb, GdSb, and YSb can be clearly seen in Figs. 1(a)–1(c). Panels (c)–(f) show the ARPES intensity along the red dashed lines in Fig. 3(b). The corresponding momentum dispersion curves (MDCs) at the chemical potential are shown at the top subpanels of the ARPES intensity plot, with green arrows pointing to the peak positions of each visible Fermi crossing. Cut no. 1 illustrates the cut along the Γ-X-Γ direction. At least one electron pocket is clearly seen at the center (X point) and two hole pockets at the edge (Γ point) of the plot. Four peaks (corresponding to Fermi crossings) at the X point can be seen in the MDCs in the top subpanel (c), demonstrating that there are two electron pockets at the X point. The red dashed lines are the results of the band-structure calculations using the FPLAPW method, which matches relatively well with the ARPES measurements. We should note that there are three hole bands and one electron band crossing the Fermi level at the Γ point in the band-structure calculations. However, in most of the compounds that we have measured, only two hole pockets are most often visible, possibly due to the off-center k_z positions. As shown in Fig. 3(a), the calculated FS has $k_z = 0$, whereas the Fermi surfaces shown in Figs. 1(a)–1(d) have k_z values marked by the red dashed lines in Figs. 4(a)–4(d).

To determine the three-dimensionality of the electronic structure of RSb [52], it is essential to tune the incident photon energies, which tunes the out-of-plane (k_z) momentum. At ALS and SRC synchrotron light sources, we measured the band dispersion along the k_z direction using photon energies in the 20–150 eV range (Fig. 4). The inner potentials used for k_z conversions are 12 eV for Figs. 4(a)–4(c) and 64 eV for Fig. 4(d). We note that the significant difference between LuSb and the rest of the family may be due to the surface contributions, which are greatly diminished in laser ARPES measurements (more bulk sensitivity), as shown in Figs. 5 and 6. Although the Fermi surfaces of these compounds show some similarity, as shown in Fig. 1, the k_z dispersions shown in Fig. 4 display significant variations in intensity and shape. The size (cross-section area) of the Fermi surface sheets from different materials shown in Fig. 4 also varies. In panels 3(d1)–3(d4), the band structure of LuSb measured using different photon energies shows the three-dimensional character of this compound. The corresponding k_z values of Figs. 3(d1)–3(d4) are marked using red dashed lines in Fig. 4(d). At 85 and 105 eV [panels (d1) and (d2)], only one hole pocket can be easily identified. However, at 125 and 145 eV [panels (d3) and (d4)], four band crossings (i.e., two hole pockets) can be rather easily observed. Similar structures can be seen in all k_z dispersion plots.

To get more detailed information about the k_z dispersion in these compounds, we have utilized the ultrahigh-resolution, tunable laser ARPES system. We should note that due to the limited range of accessible photon energies in our laboratory-based laser source, we can only map out a portion of the Brillouin zone along the k_z direction. Figure 5(a) shows the ARPES intensity of YSb close to the Γ point measured using various photon energies from 5.54 to 6.05 eV. The band dispersion clearly shifts upward as incident photon energies are lowered, and it touches the Fermi level at an incident photon energy of 5.9 eV. At a photon energy of 5.54 eV, clear Fermi crossings are observed. Thus, the hole band close to the Γ point in YSb reveals expected strong three-dimensionality. This result is consistent with the band-structure calculations

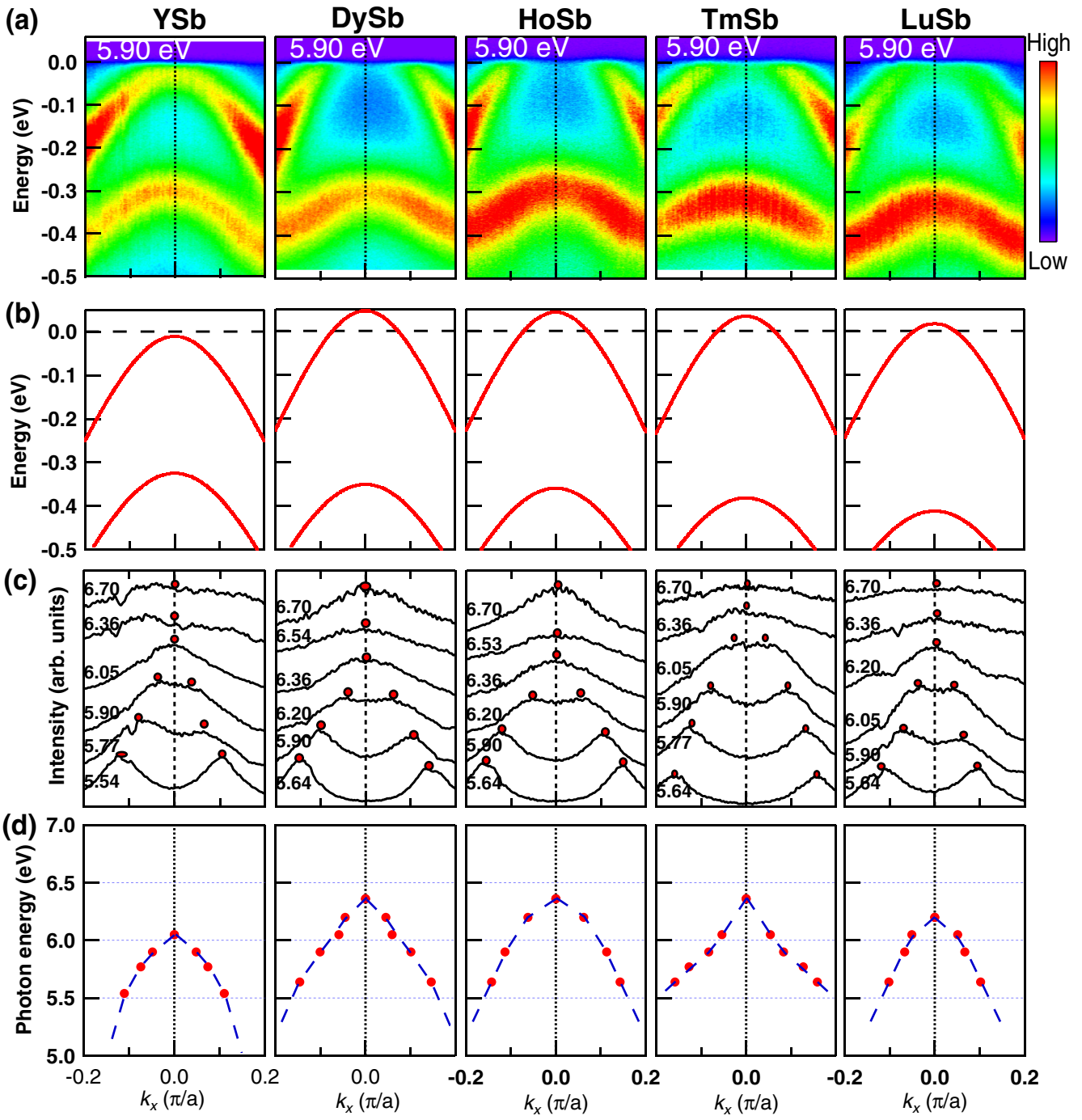

FIG. 6. Band dispersion of *R*Sb at the Γ point measured at $T = 40$ K and using different photon energies. (a) Band dispersion of *R*Sb ($R =$ Y, Dy, Ho, Tm, and Lu, from left to right, respectively) measured using a photon energy of 5.90 eV. (b) Calculated band dispersion of *R*Sb ($R =$ Y, Dy, Ho, Tm, and Lu, from left to right, respectively) at $k_z = 0.28(2\pi/c)$. (c) MDCs at E_F measured using different photon energies. The photon energies are marked on the left-hand side of the corresponding MDCs. The red solid dots mark the peak positions of the MDCs. (d) k_z dispersion of *R*Sb ($R =$ Y, Dy, Ho, Tm, and Lu, from left to right, respectively) extracted from panel (c). The red solid dots are reproduced from panel (c) with each photon energy marked on the left-hand side of the MDCs. The blue dashed lines are guides to the eye.

shown in Fig. 5(b) at various k_z. The band dispersions in DySb, HoSb, TmSb, and LuSb all have similar structures, as shown in Fig. 6(a), except it seems that the chemical potential varies slightly for different rare-earth elements. For example, it appears that the value of the chemical potential is higher in LuSb than DySb. The shift of E_F is probably due to the difference in the size of the rare-earth ions, i.e., lanthanide contraction [53], since all the partially filled 4*f* electrons can be considered as part of the core and do not contribute much to the conduction bands of these materials. Therefore, smaller lattice constants will result in higher chemical potential. This is consistent with the electronic structure calculation results shown in Fig. 6(b). Panel (c) presents the MDCs of the corresponding materials measured using the specific photon

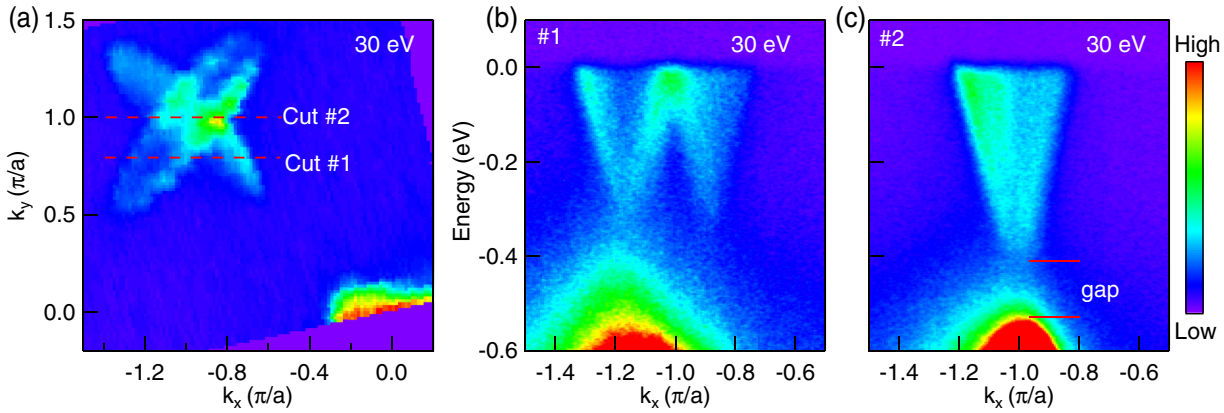

FIG. 7. Fermi surface plot and band dispersion of GdSb measured at $T = 35$ K using a photon energy of 30 eV. (a) Fermi surface plot of ARPES intensity integrated within 10 meV about the chemical potential. (b)–(c) Band dispersion along cuts 1–2.

energies at E_F. The red dots mark the peak positions of the MDCs obtained by using double Lorentzian function fits. These data clearly show that the size of the FS depends strongly on the photon energy, thus k_z. By collecting the data for all these compounds using various photon energies, we successfully determined their k_z dispersion shown in panel (d). The red solid dots in panel (d) represent the peak positions of the MDCs as shown in panel (c). The blue dashed lines are guides to the eye and clearly reveal shapes of the Fermi surface along the k_z direction.

As previously discussed, CeSb and GdSb have large magnetoresistance. Thus we will discuss the electronic structure of these compounds in more detail (YSb was found to have large magnetoresistance recently [54–56], and the interplay between substantial carrier mobility and moderate charge compensation may be the mechanism behind the large magnetoresistance [57]). As was demonstrated in Fig. 3(c), the two intersecting electron pockets at the X point cannot be easily resolved from the band dispersion in LuSb. To demonstrate that there are indeed two electron pockets at the X point, we have plotted the enhanced diagram around the X point for GdSb that was measured using a photon energy of 30 eV in Fig. 7. Panels (b) and (c) show the band dispersion along cuts no. 1 and no. 2. In Fig. 7(b), two electron pockets can be clearly seen, showing a "W"-like shape. However, the last part of the "W" is not very visible, probably due to the matrix elements effect. Panel (c) presents the band dispersion along cut no. 2 in (a), and it demonstrates that the two electron bands in panel (b) are degenerate, with a visible gap between the upper and lower bands. These results confirm that there are indeed two electron pockets at the X point with a gap between the conduction and valence bands. Upon the completion of this work, we noticed that a similar structure is also reported in CeSb, where a new type of fourfold-degenerate fermions was proposed [41].

To answer the question of whether other rare-earth monoantimonides host such fourfold-degenerate states, we have plotted the FS and high-symmetry cuts along the Γ-X direction from CeSb, GdSb, and YSb in Fig. 8. In CeSb [panel (a)], the two intersecting electron bands seem to be touching the top of the lower bands, consistent with the results from Ref. [41]. However, in YSb and GdSb, there is a significant gap (so significant that we cannot see the lower band in this energy range) between the electron pockets and the lower hole bands,

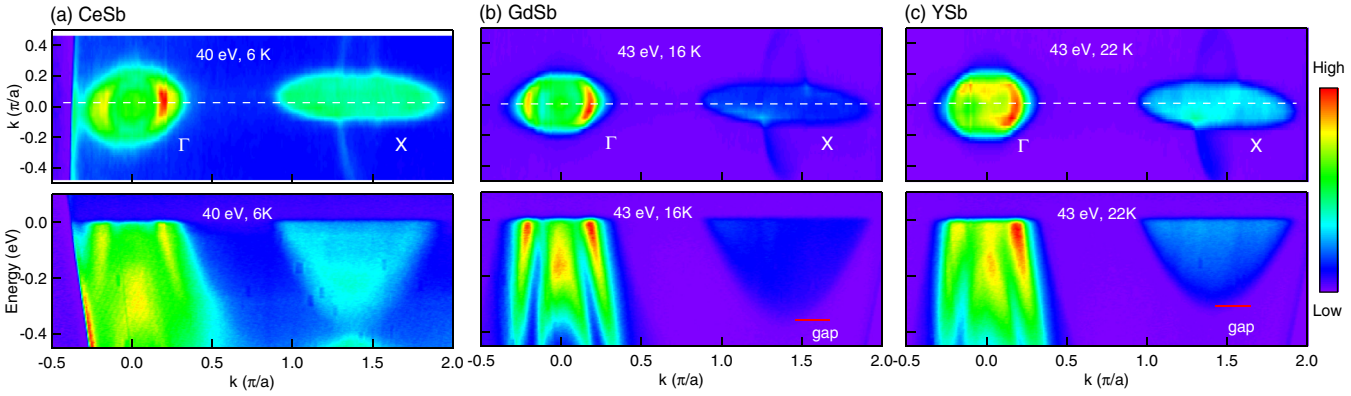

FIG. 8. FS and high-symmetry cuts (along the white dashed lines in each FS plot) of CeSb, GdSb, and YSb. (a) FS and band dispersion of CeSb measured using a photon energy of 40 eV and $T = 6$ K. (b) FS and band dispersion of GdSb measured using a photon energy of 43 eV and $T = 16$ K. (c) FS and band dispersion of YSb measured using a photon energy of 43 eV and $T = 22$ K.

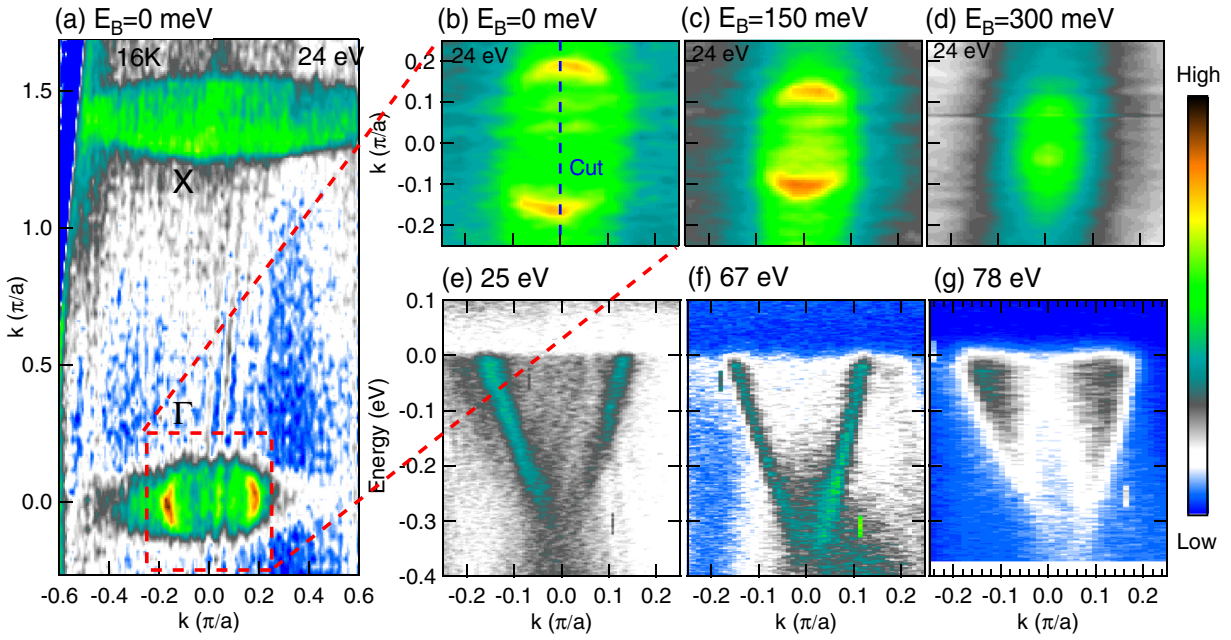

FIG. 9. FS and high-symmetry cuts of GdSb. (a) FS of GdSb measured using a photon energy of 24 eV. (b) FS (rotated 90°) of the zoom in area in (a). (c) Constant energy contour plot at a binding energy of 150 meV. (d) Constant energy contour plot at a binding energy of 300 meV. (e) Band dispersion along the cut as shown in (b) measured using a photon energy of 25 eV. (f) The same cut as in (e) measured using a photon energy of 67 eV. (g) The same cut as in (e) measured using a photon energy of 78 eV.

as seen from the band dispersion along the high-symmetry cuts.

What is interesting is that similar to the results in LaBi [58], we have also observed a Dirac-like electron band at the Γ point in YSb, CeSb, and GdSb for some specific values of photon energy. The details of the Dirac-like band in GdSb are shown in Fig. 9. Panel (a) shows the FS of GdSb measured using a photon energy of 24 eV. The zoom-in image of the red box in (a) is presented in (b). Panel (c) shows the constant energy contour plot at a binding energy of 150 meV, where we can still recognize the circular shape. The constant energy contour plot at a binding energy of 300 meV is shown in (d), showing that the electron pocket shrinks down to a single point at the center. Panels (e)–(g) show the high-symmetry cut [as marked in (b)] measured using some photon energies, which shows rather linear dispersive bands. This Dirac-like structure may contribute to the unusually high magnetoresistance in these materials [24,54–56,59].

IV. CONCLUSION

The *R*Sb family is an ideal system for studying the evolution of electronic structure due to different rare-earth ions. We successfully measured the FS of rare-earth monoantimonides with $R =$ Y, Ce, Gd, Dy, Tm, Ho, and Lu by using synchrotron radiation and laser-based ARPES systems. Fermi surfaces of different materials measured using different photon energies show a similar structure of at least two hole pockets centered at the Γ point and two intersecting electron pockets at the X points. The results match relatively well with the band-structure calculations. By using the synchrotron and tunable VUV laser ARPES systems, we mapped the k_z dispersion of *R*Sb and concluded that the inner hole band centered at the Γ point has strong three-dimensionality. By comparing the band structure for different rare-earth elements, we show that the 4*f* electrons in these ions do not qualitatively affect the electronic structure close to the chemical potential. The ion size (because of lanthanide contraction), on the other hand, has a significant effect on the chemical potential in these materials. With a smaller crystal lattice, the chemical potential moves higher. The lanthanide contraction effect has been demonstrated by both ARPES measurements and electronic structure calculations. Though our instrumentation has limited our ability to probe the low-temperature phase transitions of DySb and CeSb, our results provide insight into the basic electronic structures of these materials. Further research is needed, especially measurements carried out at lower temperatures to study the magnetic phase transitions in these materials.

ACKNOWLEDGMENTS

We would like to thank Xin Zhao for helpful discussions. This work was supported by the US Department of Energy (DOE), Office of Science, Basic Energy Sciences, Materials Science and Engineering Division. The research was performed at the Ames Laboratory, which is operated for the U.S. DOE by Iowa State University under Contract No. DE-AC02-07CH11358. Y.W. (analysis of ARPES data) was supported by Ames Laboratory's Laboratory-Directed Research and Development (LDRD) funding. L.H. was supported by CEM, a NSF MRSEC, under Grant No. DMR-1420451.

Raw data for this manuscript are available at http://lib.dr.iastate.edu/ameslab_datasets/.

[1] H. R. Child, M. K. Wilkinson, J. W. Cable, W. C. Koehler, and E. O. Wollan, Phys. Rev. **131**, 922 (1963).

[2] G. Busch, O. Marinček, A. Menth, and O. Vogt, Phys. Lett. **14**, 262 (1965).

[3] B. R. Cooper and O. Vogt, Phys. Rev. B **1**, 1211 (1970).

[4] J. Rossat-Mignod, P. Burlet, J. Villain, H. Bartholin, W. Tcheng-Si, D. Florence, and O. Vogt, Phys. Rev. B **16**, 440 (1977).

[5] C.-G. Duan, R. F. Sabirianov, W. N. Mei, P. A. Dowben, S. S. Jaswal, and E. Y. Tsymbal, J. Phys.: Condens. Matter **19**, 315220 (2007).

[6] G. Busch and O. Vogt, J. Appl. Phys. **39**, 1334 (1968).

[7] E. Bucher, R. J. Birgeneau, J. P. Maita, G. P. Felcher, and T. O. Brun, Phys. Rev. Lett. **28**, 746 (1972).

[8] T. Wiener and P. Canfield, J. Alloys Compd. **303-304**, 505 (2000).

[9] R. Pittini, J. Schoenes, O. Vogt, and P. Wachter, Phys. Rev. Lett. **77**, 944 (1996).

[10] E. Mun, H. Ko, G. J. Miller, G. D. Samolyuk, S. L. Bud'ko, and P. C. Canfield, Phys. Rev. B **85**, 035135 (2012).

[11] M. N. Ali, J. Xiong, S. Flynn, J. Tao, Q. D. Gibson, L. M. Schoop, T. Liang, N. Haldolaarachchige, M. Hirschberger, N. P. Ong, and R. J. Cava, Nature (London) **514**, 205 (2014).

[12] T. Liang, Q. Gibson, M. N. Ali, M. Liu, R. J. Cava, and N. P. Ong, Nat. Mater. **14**, 280 (2015).

[13] A. Narayanan, M. D. Watson, S. F. Blake, N. Bruyant, L. Drigo, Y. L. Chen, D. Prabhakaran, B. Yan, C. Felser, T. Kong, P. C. Canfield, and A. I. Coldea, Phys. Rev. Lett. **114**, 117201 (2015).

[14] Y. Wu, L. Wang, E. Mun, D. D. Johnson, D. Mou, L. Huang, Y. Lee, S. L. Bud'ko, P. C. Canfield, and A. Kaminski, Nat. Phys. **12**, 667 (2016).

[15] A. A. Soluyanov, D. Gresch, Z. Wang, Q. Wu, M. Troyer, X. Dai, and B. A. Bernevig, Nature (London) **527**, 495 (2015).

[16] F. Y. Bruno, A. Tamai, Q. S. Wu, I. Cucchi, C. Barreteau, A. de la Torre, S. McKeown Walker, S. Riccò, Z. Wang, T. K. Kim, M. Hoesch, M. Shi, N. C. Plumb, E. Giannini, A. A. Soluyanov, and F. Baumberger, Phys. Rev. B **94**, 121112(R) (2016).

[17] C. Wang, Y. Zhang, J. Huang, S. Nie, G. Liu, A. Liang, Y. Zhang, B. Shen, J. Liu, C. Hu, Y. Ding, D. Liu, Y. Hu, S. He, L. Zhao, L. Yu, J. Hu, J. Wei, Z. Mao, Y. Shi, X. Jia, F. Zhang, S. Zhang, F. Yang, Z. Wang, Q. Peng, H. Weng, X. Dai, Z. Fang, Z. Xu, C. Chen, and X. J. Zhou, Phys. Rev. B **94**, 241119 (2016).

[18] Y. Wu, D. Mou, N. H. Jo, K. Sun, L. Huang, S. L. Bud'ko, P. C. Canfield, and A. Kaminski, Phys. Rev. B **94**, 121113 (2016).

[19] B. Feng, Y.-H. Chan, Y. Feng, R.-Y. Liu, M.-Y. Chou, K. Kuroda, K. Yaji, A. Harasawa, P. Moras, A. Barinov, W. Malaeb, C. Bareille, T. Kondo, S. Shin, F. Komori, T.-C. Chiang, Y. Shi, and I. Matsuda, Phys. Rev. B **94**, 195134 (2016).

[20] Z. Wang, H. Weng, Q. Wu, X. Dai, and Z. Fang, Phys. Rev. B **88**, 125427 (2013).

[21] M. Neupane, S. Xu, R. Sankar, N. Alidoust, G. Bian, C. Liu, I. Belopolski, T. Chang, H. Jeng, H. Lin, A. Bansil, F. Chou, and M. Z. Hasan, Nat. Commun. **5**, 3786 (2014).

[22] Z. K. Liu, J. Jiang, B. Zhou, Z. J. Wang, Y. Zhang, H. M. Weng, D. Prabhakaran, S.-K. Mo, H. Peng, P. Dudin, T. Kim, M. Hoesch, Z. Fang, X. Dai, Z. X. Shen, D. L. Feng, Z. Hussain, and Y. L. Chen, Nat. Mater. **13**, 677 (2014).

[23] S. Borisenko, Q. Gibson, D. Evtushinsky, V. Zabolotnyy, B. Büchner, and R. J. Cava, Phys. Rev. Lett. **113**, 027603 (2014).

[24] D. X. Li, Y. Haga, H. Shida, T. Suzuki, and Y. S. Kwon, Phys. Rev. B **54**, 10483 (1996).

[25] A. Hasegawa and A. Yanase, J. Phys. Soc. Jpn. **42**, 492 (1977).

[26] A. Hasegawa, J. Phys. C **13**, 6147 (1980).

[27] A. Hasegawa, J. Phys. Soc. Jpn. **54**, 677 (1985).

[28] A. I. Liechtenstein, V. P. Antropov, and B. N. Harmon, Phys. Rev. B **49**, 10770 (1994).

[29] H. M. Tütüncü, S. Bagci, and G. P. Srivastava, J. Phys.: Condens. Matter **19**, 156207 (2007).

[30] P. Rodríguez-Hernández and A. Muñoz, Int. J. Quantum Chem. **101**, 770 (2005).

[31] P. Larson, S. D. Mahanti, S. Sportouch, and M. G. Kanatzidis, Phys. Rev. B **59**, 15660 (1999).

[32] N. Singh, S. M. Saini, T. Nautiyal, and S. Auluck, J. Phys.: Condens. Matter **19**, 346226 (2007).

[33] H. Kitazawa, Y. Kwon, A. Oyamada, N. Takeda, H. Suzuki, S. Sakatsume, T. Satoh, T. Suzuki, and T. Kasuya, J. Magn. Magn. Mater. **76-77**, 40 (1988).

[34] R. Settai, T. Goto, S. Sakatume, Y. Kwon, T. Suzuki, Y. Kaneta, and O. Sakai, J. Phys. Soc. Jpn. **63**, 3026 (1994).

[35] C. G. Olson, P. J. Benning, M. Schmidt, D. W. Lynch, P. Canfield, and D. M. Wieliczka, Phys. Rev. Lett. **76**, 4265 (1996).

[36] H. Kumigashira, H.-D. Kim, A. Ashihara, A. Chainani, T. Yokoya, T. Takahashi, A. Uesawa, and T. Suzuki, Phys. Rev. B **56**, 13654 (1997).

[37] H. Kumigashira, H.-D. Kim, T. Ito, A. Ashihara, T. Takahashi, T. Suzuki, M. Nishimura, O. Sakai, Y. Kaneta, and H. Harima, Phys. Rev. B **58**, 7675 (1998).

[38] H. Kumigashira, H.-D. Kim, T. Ito, A. Ashihara, T. Takahashi, H. Aoki, A. Ochiai, and T. Suzuki, Physica B **259-261**, 1124 (1999).

[39] H. Kumigashira, T. Ito, A. Ashihara, H.-D. Kim, H. Aoki, T. Suzuki, H. Yamagami, T. Takahashi, and A. Ochiai, Phys. Rev. B **61**, 15707 (2000).

[40] A. Takayama, S. Souma, T. Sato, T. Arakane, and T. Takahashi, J. Phys. Soc. Jpn. **78**, 073702 (2009).

[41] N. Alidoust, A. Alexandradinata, S.-Y. Xu, I. Belopolski, S. K. Kushwaha, M. Zeng, M. Neupane, G. Bian, C. Liu, D. S. Sanchez *et al.*, arXiv:1604.08571.

[42] M. Abdusalyamova, H. Shokirov, and O. Rakhmatov, J. Less-Common Met. **166**, 221 (1990).

[43] Y. Jia, J. Solid State Chem. **95**, 184 (1991).

[44] http://abulafia.mt.ic.ac.uk/shannon/radius.php?Element=Y, accessed: 2017-3-1.

[45] N. Nereson and V. Struebing, AIP Conf. Proc., **5**, 1385 (1972).

[46] P. C. Canfield and Z. Fisk, Philos. Mag. B **65**, 1117 (1992).

[47] P. C. Canfield and I. R. Fisher, J. Cryst. Growth **225**, 155 (2001).

[48] P. Blaha, K. Schwarz, G. K. H. Madsen, D. Kvasnicka, and J. Luitz, *WIEN2K, An Augmented Plane Wave + Local Orbitals Program for Calculating Crystal Properties* (Techn. Universität Wien, Austria, 2001).

[49] J. P. Perdew, K. Burke, and M. Ernzerhof, Phys. Rev. Lett. **77**, 3865 (1996).

[50] R. Jiang, D. Mou, Y. Wu, L. Huang, C. D. McMillen, J. Kolis, Henry G. Giesber III, J. J. Egan, and A. Kaminski, Rev. Sci. Instrum. **85**, 033902 (2014).

[51] M. Zeng, C. Fang, G. Chang, Y.-A. Chen, T. Hsieh, A. Bansil, H. Lin, and L. Fu, arXiv:1504.03492.

[52] S. Hüfner, *Photoelectron Spectroscopy: Principles and Applications* (Springer-Verlag, Berlin, 1996).
[53] K. N. R. Taylor and M. I. Darby, *Physics of Rare Earth Solids* (Chapman and Hall, London, 1972).
[54] N. J. Ghimire, A. S. Botana, D. Phelan, H. Zheng, and J. F. Mitchell, J. Phys.: Condens. Matter **28**, 235601 (2016).
[55] Q.-H. Yu, Y.-Y. Wang, S. Xu, and T.-L. Xia, arXiv:1604.05912.
[56] O. Pavlosiuk, P. Swatek, and P. Wiśniewski, Sci. Rep. **6**, 38691 (2016).
[57] J. He, C. Zhang, N. J. Ghimire, T. Liang, C. Jia, J. Jiang, S. Tang, S. Chen, Y. He, S.-K. Mo, C. C. Hwang, M. Hashimoto, D. H. Lu, B. Moritz, T. P. Devereaux, Y. L. Chen, J. F. Mitchell, and Z.-X. Shen, Phys. Rev. Lett. **117**, 267201 (2016).
[58] Y. Wu, T. Kong, L.-L. Wang, D. D. Johnson, D. Mou, L. Huang, B. Schrunk, S. L. Bud'ko, P. C. Canfield, and A. Kaminski, Phys. Rev. B **94**, 081108 (2016).
[59] T. Kasuya, M. Sera, Y. Okayama, and Y. Haga, J. Phys. Soc. Jpn. **65**, 160 (1996).